

Excimer Laser Photofragmentation/Fragment Detection for Analysis of the Oxygenated Hydrocarbon Ethyl-3-Ethoxypropionate: Implications for Atmospheric Monitoring

P. S. DALYANDER and D. W. HAHN*

Department of Mechanical and Aerospace Engineering, University of Florida, Gainesville, Florida 32611

In the present study, the use of ArF excimer laser photofragmentation/fragment detection (PF/FD) is considered for the characterization of gaseous ethyl-3-ethoxypropionate (EEP), a representative solvent within the class of oxygenated volatile organic compounds (VOCs). PF/FD measurements of EEP resulted in identification of the resulting photofragments as C₂ and CH, allowing photofragmentation pathways to be proposed for the parent molecule for the first time. In addition, PF/PD measurements of EEP recorded in the presence of sodium-based aerosol particles resulted in a reduced signal from the EEP, indicating adsorption onto the particulates, thereby demonstrating proof-of-concept that PF/FD can be used to study heterogeneous chemical reactions relevant to atmospheric chemistry. Finally, both time-integrated and time-resolved measurements of the EEP photofragmentation signal in varying concentrations of oxygen revealed that oxygen effectively acts as a dynamic quencher of the EEP signal. In consideration of oxygen quenching, care must be taken in calibrating/analyzing data in selected applications of PF/FD for VOC characterization (such as combustion emission monitoring) in order to account for the potential variability of oxygen concentration.

Index Headings: **Photofragmentation; Fragment detection; Volatile organic compounds; Ethyl-3-ethoxypropionate; Oxygenated hydrocarbon; Quenching; Heterogeneous chemistry.**

INTRODUCTION

Volatile organic compounds (VOCs), including oxygenated hydrocarbons, are a class of gaseous pollutants known to have detrimental effects on both the environment and human health through indoors and outdoors exposure. Increased concentrations of VOCs have been linked with increased rates of cancer of the brain, nervous system, skin, and endocrine system,¹ while high indoor concentrations have been linked to "sick building syndrome" and increased risk of lung cancer.² Many VOCs undergo photochemical reactions in the troposphere, producing the secondary pollutant ozone, which in the short term has been linked with increased mortality rates in urban centers and in the long term has been linked to increased risk of asthma and lung disease.³ VOCs are generated from a variety of sources and can be found in household chemicals, paints, solvents, and adhesives, as well as a range of industrial sources.⁴ In addition, VOCs, such as benzene, acetaldehyde, and formaldehyde, as well as unburned hydrocarbons, are found in significant quantities in combustion exhaust from both stationary and mobile sources.⁵ Because of the wide range of sources of VOCs and their threat to the atmosphere and human health, it is imperative that quantification and characterization methods be developed that are accurate and allow rapid, preferably real-time, analysis. One technique that is largely

unexplored for this application and that potentially meets these criteria is excimer laser photofragmentation/fragment detection (PF/FD).

The PF/FD technique is an optical technique wherein a laser with high photon energy (e.g., excimer laser) is used to dissociate some bonds in a target molecule or compound, leaving the resultant photofragments in an excited state, which subsequently decay back to the ground state via fluorescence at a wavelength characteristic of the transient species.⁶⁻⁸ The wavelength of the incident laser must overlap with an absorption feature of the target molecule, although not necessarily resonant to an electronic state, and the photon energy ($h\nu$) must be sufficient to dissociate the target molecule and leave the resulting fragments in an excited state. Unlike the case of laser-induced breakdown spectroscopy (LIBS), there is insufficient energy density to cause breakdown and subsequent plasma formation, nor to completely atomize/ionize all molecules within the target volume.^{6,7} This characteristic of PF/PD allows some molecular information (i.e., chemical structure) to be retained and facilitates the identification of large, complicated species (such as complex hydrocarbons and VOCs) for which basic elemental data (e.g., via atomic emission) may be insufficient for robust identification.⁹

Once target molecules have been photolyzed, the resultant fragments may be detected using one of several optical techniques, including laser-induced fluorescence (LIF), photoionization (PI), laser ionization recombination emission (LIRE), and prompt photoionization or prompt emission (PPI or PE).⁸ In the case of the first three detection techniques, a second laser pulse is required to cause optical emission by the photofragments and thus allow their detection. Depending on the absorption characteristics of the target molecules, the wavelength of this secondary pulse may be coincident with the photofragmenting wavelength, and thus the same laser may be used for both processes. In the case of prompt emission, however, sufficient excess energy exists within the molecular fragments to leave them in an excited state, which may then spontaneously decay and emit light characteristic of the fragment species.⁸ In the present study, PF/FD with prompt emission is used as the analytical technique. In simple molecules with bond energies sufficiently low enough to allow dissociation, excess energy may be stored by exciting one or more electrons to a higher electronic state, which can subsequently relax via a radiative process, thereby emitting light at a wavelength unique to that molecular or atomic transition (i.e., $X^* \rightarrow h\nu$). For more complex molecules, the parent molecule may fragment into smaller molecules rather than atomic species, with excess energy stored into one or more of the remaining bonds, which subsequently emits light at a wavelength characteristic of the overall molecular structure.

The PF/FD technique has shown promise for qualitative and

Received 28 March 2008; accepted 19 June 2008.

* Author to whom correspondence should be sent. E-mail: dwhahn@ufl.edu.

quantitative analysis in a variety of applications, including, for example, the detection of vaporous hydrogen peroxide,¹⁰ monitoring of gas-phase alkalis in coal plant exhaust to reduce fouling,^{11–14} quantification of lead (in both particulate and vaporous form) as an environmental pollutant,¹⁵ detection of the photochemical smog/acid rain contributing species NO₂ and NO,¹⁶ environmental monitoring of chlorinated hydrocarbons,¹⁷ and analysis of atmospheric ammonia.^{18–21} Photo-fragmentation has also been used for the detection and quantification of several types of particulate species, such as the air pollutants ammonium nitrate and ammonium sulfate,²² carbonaceous particles and soot generated by combustion,^{22,23} and a variety of sodium-containing aerosol particles.^{24–26} Like many laser spectroscopic techniques, PF/FD offers significant advantages over traditional off-line methods of chemical analysis in that it provides nearly instantaneous results with a high degree of species differentiation.^{7,8} PF/FD is particularly useful for analyzing molecules unsuited for detection with other, direct methods of spectroscopic analysis; for example, PF/FD is applicable to molecules with weak optical transitions or broad spectral features when probed using direct detection methods such as laser-induced fluorescence (LIF), photoionization, and absorption.^{7,8} Although the analyte itself may contain poorly defined spectral features, the photofragmentation products are smaller molecules or atoms that are generally more easily identified and as such can be used to reconstruct the parent species. Because some molecular data is retained, PF/FD is also suitable for complex molecules where identification via pure atomic spectroscopy techniques is poorly suited.

In the present study, the use of PF/FD for the characterization and monitoring of gas-phase volatile organic compounds, specifically oxygenated hydrocarbons, will be considered. Very limited work has been carried out using PF/FD for detecting this type of complex species, with research restricted to studies of carbonaceous particle/vapor systems such as are found in combustion emission²² and the monitoring of chlorinated hydrocarbons.¹⁷ In this case, the technique will be tested for the detection of a representative solvent, gaseous ethyl-3-ethoxypropionate (EEP), a pollutant found in paint thinner and used in particularly high volume for the stripping of aircraft paint by the U.S. Air Force.²⁷ In addition to the use of PF/FD for the characterization of EEP, the technique will be applied to systems containing both EEP and an aerosol to determine whether it is applicable for the determination of adsorption of the vapor-phase EEP onto the particulate phase, thereby serving as a tool for the study of heterogeneous atmospheric chemical reactions involving VOCs or other gases.

EXPERIMENTAL CONFIGURATION AND METHODS

The experimental design is shown in Fig. 1a. The configuration consists of a supply line of purified dry air or purified nitrogen, or a mixture of nitrogen and oxygen in a controlled volumetric ratio. The gas lines are split, with separate controlled flows running to (1) a bubbler (for introduction of EEP), (2) a diluting/drying co-flow stream, and (3) a nebulizer for aerosol generation. The mass flow rate of each of the gas streams was controlled with precision mass flow controllers (MFCs) with an accuracy of 1% of full scale and a repeatability of 0.5% of full scale. Each flow controller was sized to the appropriate range: 0–1 SLPM on the bubbler

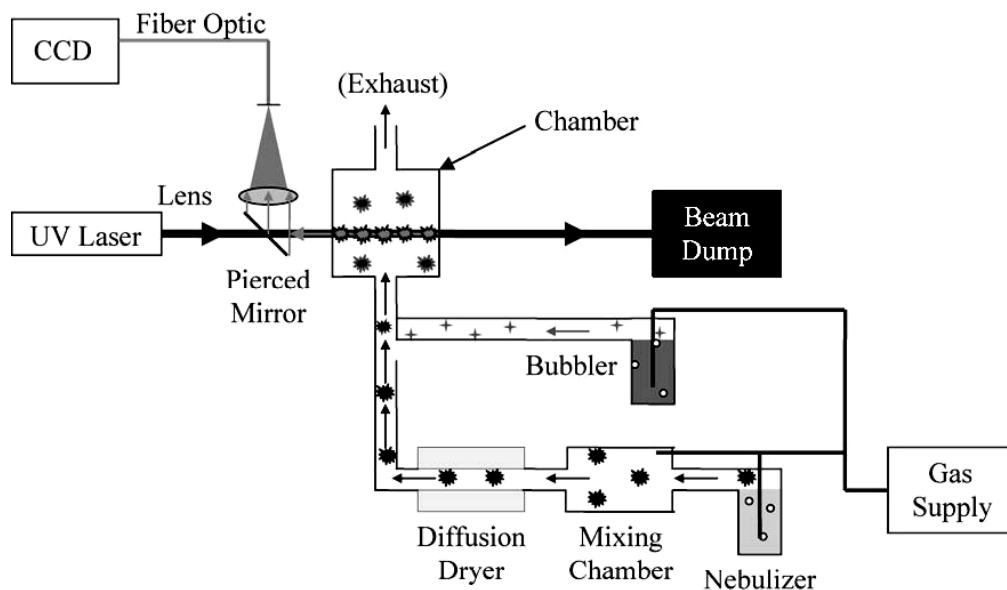
line controller, 0–5 SLPM on the nebulizer line controller, and two 0–10 SLPM MFC units in parallel for the co-flow stream, yielding a total co-flow rate of 20 SLPM.

Aerosol species were generated using a TSI Model 3076 Constant Output Atomizer. The atomizer consists of a reservoir containing the analyte of interest in a solution of ultra-purified deionized water. As gas flows over the inlet tube from the reservoir, liquid is drawn upward and sprayed in a fine jet into the outlet tube. Large droplets impact the inner walls of the housing and return back to the reservoir, leaving only fine droplets to continue on through the system. The concentration of analyte within the nebulized solution controls the size distribution of the resultant aerosol particle following droplet desolvation. As implemented in the present study, the resulting solid particulates have mean diameters less than 100 nm.²⁸ In order to minimize the effects of liquid water on the laser/analyte interaction, the output from the nebulizer was mixed with a dry co-flow gas stream in a mixing chamber (serving to both dry and dilute the stream), and further dried by passing through a diffusion dryer consisting of a perforated gas flow tube embedded in silica desiccant. The resulting system is designed to produce a very dry, sub-micrometer-sized aerosol.

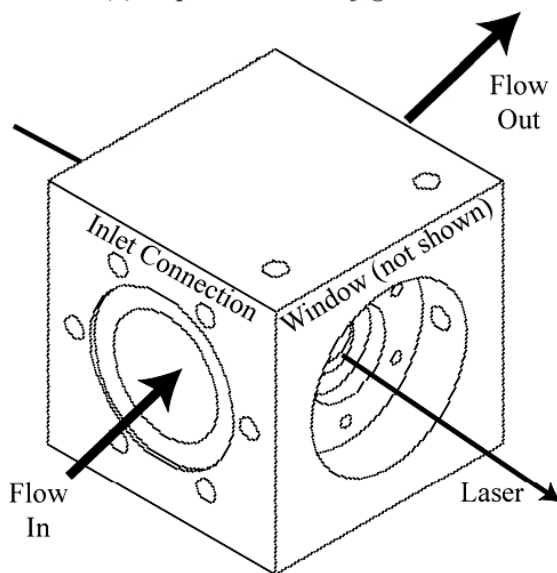
A bubbler consisting of a sealed PVC reservoir was used to introduce gaseous EEP into the gas stream. The top cap of the reservoir accommodated the insertion of a rigid 6.3 mm stainless steel tube running to the bottom of the liquid reservoir (comprising the bubbler inlet) and a shorter 6.3 mm tube terminating in the top of the bubbler (comprising the outlet side). Gas flowing through the inlet tube produces bubbles within the liquid reservoir that infuse with vaporous EEP as they rise to the surface, thereby producing an EEP-doped gas flow. Valves at the inlet and outlet of the bubbler allowed this apparatus to be readily shut-off and sealed from the sample chamber for experimentation without the presence of EEP vapor.

The output from the nebulizer and the bubbler flowed into the sample chamber, shown in Fig. 1b, where photofragmentation occurs. In this design, a solid stainless steel cube was bored out with a tube of the same diameter as the gas inlet and outlet tubes such that flow proceeds directly through the chamber without any additional residence time. Optical access was achieved orthogonal to the flow direction via inset optical windows held in place by Teflon o-rings clamped down by stainless steel flanges. These windows were made of high transmission Suprasil UV grade quartz. Despite the use of UV grade quartz, the close proximity of the windows to the focal point of the laser resulted in some loss of laser transmission over time. To avoid drift in optical transmission over different experiments, the optical access windows were cleaned between subsequent runs to minimize the presence of aerosol particle build-up. In addition, the cube was oriented so that inlet flow entered from the top of the chamber and exhausted out through the bottom, thereby eliminating gravitational settling on the lower chamber walls. Finally, the cube was electrically grounded to earth to minimize electrostatic loss of the aerosol particles to the chamber walls, noting that the particles incur a small charge during the nebulization process. After passing through the sample chamber, the gas/aerosol stream was vented through an exhaust system.

The photofragmentation laser was an ArF excimer laser (GAM laser, EX5) operating at a wavelength of 193 nm and repetition rate of 50 Hz. The laser passed through a pierced mirror and a lens that focused the beam to the center of the



(a) Experimental configuration



(b) Cube chamber design

Fig. 1. (a) Schematic of the photofragmentation experimental test configuration, and (b) schematic diagram of the modified sample chamber cube.

sample chamber. The pulse energy entering the sample chamber was kept constant at 0.83 mJ per pulse. Within the chamber, the energy flux of the laser is calculated as 2.6 J/cm^2 , based on the incident energy and approximate beam diameter. A beam dump was placed to capture excess laser energy that passed through the chamber (see Fig. 1). Light emitted via photofragmentation passed through the incident chamber window and was reflected by the pierced mirror to a 4-in. diameter focusing lens that directed the light onto a fiber-optic bundle. The optical transmission through the focusing lens (borosilicate crown optical glass) is specified as 82% transmission at 400 nm, 60% transmission at 350 nm, and below 10% for wavelengths less than 300 nm. The fiber bundle was coupled to a 0.3 m Czerny–Turner spectrometer, with light recorded with an intensified charged-coupled device (iCCD)

array. Both the laser and the iCCD were triggered using a digital delay generator, with the iCCD trigger set to center the 300 ns detector gate on the actual laser pulse. The output spectra from the spectrometer in the wavelength range of interest for the target species were captured and summed over 200 acquisitions for each individual measurement.

To calculate the intensity of the emission peaks of interest, the background intensity (i.e., identical settings but with no analyte) was recorded and subtracted from the emission spectra recorded in the presence of the targeted analyte, as described below. For the two-phase measurements (i.e., aerosol particulates and EEP vapor), the nebulizer was operated with only purified, deionized water to obtain the baseline EEP signals (i.e., no aerosol present), thereby ensuring no effects from the water phase of the nebulization process.

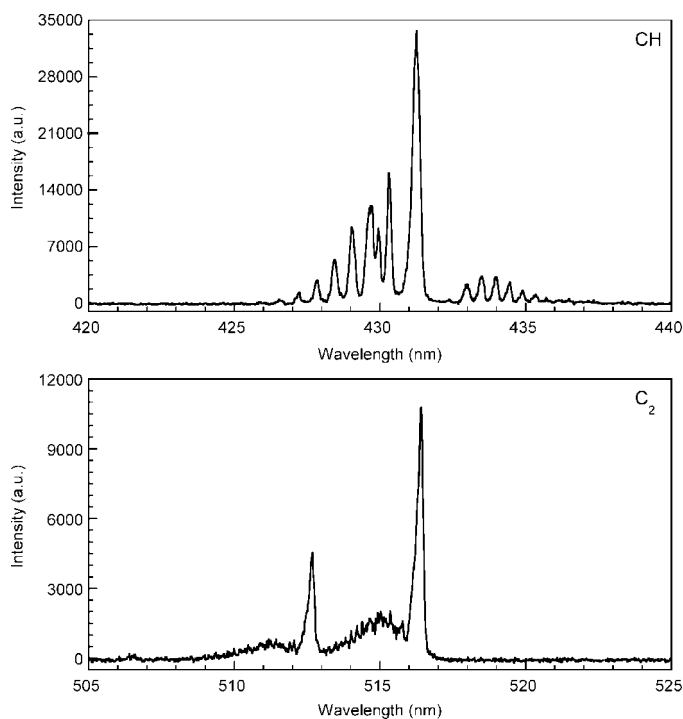


FIG. 2. ArF excimer laser photofragmentation spectra of EEP recorded in nitrogen showing (top) the CH and (bottom) the C₂ emission bands.

For processing the spectral data, blank spectra (I_{blank}) were scaled to the analyte-containing spectra ($I_{\text{signal,raw}}$) and subsequently subtracted to yield the absolute analyte spectra:

$$I_{\text{signal}} = I_{\text{signal,raw}} - I_{\text{blank}} \cdot (\text{Scale factor}) \quad (1)$$

where the scale factor is defined by the scaling of the off-peak (i.e., background signal) spectral region of the blank to the analyte-containing spectrum. Using the resulting spectra, the integrated intensity value for each wavelength of interest was then calculated by summing the intensity values over the full peak width of each analyte emission line.

In addition to the integrated intensity measurements, time-resolved photofragmentation data were collected. For these experiments, the spectral signal was recorded using the spectrometer in a monochromator mode with a fast-rise time PMT (<1 ns) and a digital oscilloscope (4 GS/s). The oscilloscope was triggered by a fast rise-time (200 ps) phototube that sampled a portion of the 193 nm incident beam. To calibrate for the difference in optical path between the phototube and PMT, as well as optical signal transmission (i.e., fiber to PMT) and electronic signal (i.e., PMT to oscilloscope), additional measurements were made by moving the phototube to equal the exact distance from the sample chamber to the fiber optic. By directly measuring the difference in delay time between the PMT and the phototube, all fluorescence lifetime measurements could be shifted with respect to the absolute temporal position of the incident laser pulse waveform, thereby allowing accurate assessment of the fluorescence lifetime.

RESULTS AND DISCUSSION

Observed EEP Photofragments. The photofragmentation of the oxygenated hydrocarbon EEP was observed to produce

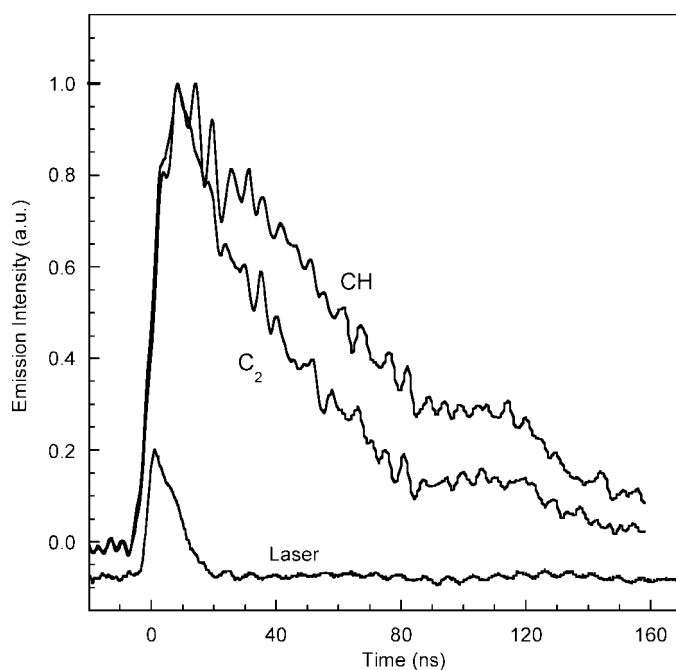


FIG. 3. Photofragmentation emission intensity as a function of time for the 516.5 nm C₂ and 431.4 nm CH molecular bands recorded in nitrogen. The emission values are each normalized to their maximum intensity. The incident ArF laser pulse waveform is shown as a reference.

fragments with excess energy that was spontaneously emitted from the newly formed molecules. Specifically, intensity peaks were observed at approximately 390 nm, multiple peaks in the region of 430–431 nm, 470 nm, 475 nm, 516 nm, and 559 nm. Note that the optics used in this experimental design prohibited the observation of any peaks with a wavelength less than approximately 350 nm; hence, this spectral region was not considered. Based on the chemical structure of EEP (C₇H₁₄O₃) (see Fig. 4 below) and known molecular band heads, all of the bands observed in the PF/FD emission structure are identified as corresponding to C₂ and CH molecules. For the present study, the strongest two CH bands at 430.4 nm ($A^2\Delta \rightarrow X^2\Pi$ 1–1) and 431.4 nm ($A^2\Delta \rightarrow X^2\Pi$ 0–0), along with the strongest observed C₂ Swan band at 516.5 nm ($A^3\Delta \rightarrow X^3\Pi$ 0–0), were considered for further quantitative analysis. Other observed bands include the CH lines at 387.1 nm ($B^2\Sigma \rightarrow X^2\Pi$ 0–0) and the additional $A^2\Delta \rightarrow X^2\Pi$ lines at 428.0, 428.7, 429.3, and 429.7 nm, and the C₂ Swan bands at 471.5 nm ($A^3\Pi_g \rightarrow X^3\Pi_u$ 2–1), 473.7 nm ($A^3\Pi_g \rightarrow X^3\Pi_u$ 1–0), and 558.7 nm ($A^3\Pi_g \rightarrow X^3\Pi_u$ 1–2). Representative example spectra recorded within these ranges for EEP are shown in Fig. 2.

In order to gain insight into the mechanisms of the photofragmentation of EEP, time-resolved measurements of the observed fluorescence intensity were recorded as described above. The time-resolved signal for the strongest band corresponding to CH photofragments (431.4 nm) and the strongest C₂ band (516.5 nm) are shown in Fig. 3, along with the reference laser pulse waveform. At all observed wavelengths, the fluorescence lifetime of the EEP photofragmentation signal is 80–100 ns, extending well past the duration of the incident laser pulse (~12 ns). This relatively long fluorescence lifetime may be indicative of a complicated photofragmentation pathway containing multiple intermediaries between the original EEP molecule and the excited CH and C₂ molecules

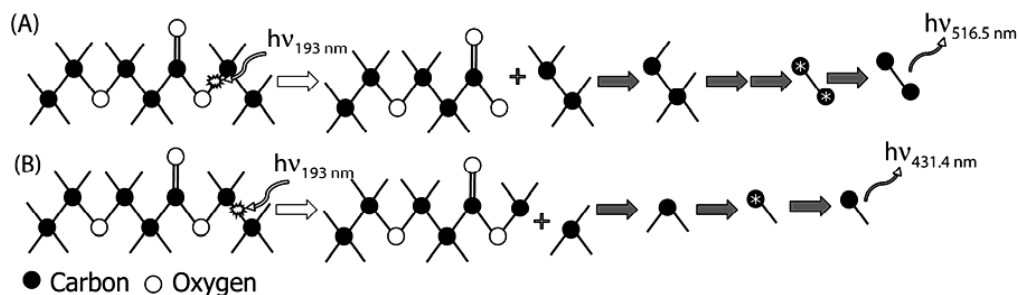


FIG. 4. Molecular structure of EEP and proposed photofragmentation pathways for emission from excited (A) C_2 and (B) CH. Intermediate H abstraction steps may be via collisional or photofragmentation processes.

that emit light at the observed wavelengths. Note that the structure observed during signal decay is not repeatable; therefore, the small intensity fluctuations are attributed to noise within the system.

Determining the effects of laser pulse energy on the observed photofragmentation signals was not a focus of the current study, although a few data points were collected. For the NaOH aerosol, both atomic sodium photofragmentation bands considered (589.0 nm and 589.6 nm) were found to vary linearly over a pulse energy range of 1.8–11 mJ. For the EEP vapor experiments, the 431.4 nm CH emission was found to vary linearly over nearly a factor of two in laser energy. While the above data do not eliminate the possibility of multiphoton processes at higher laser fluence values, the results of the current study are most likely dominated by single-photon photofragmentation processes.

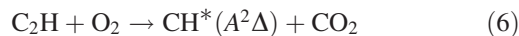
Proposed EEP Photofragmentation Pathways. Based on the molecules observed from the photofragmentation of EEP, it is possible to propose several mechanisms of fragmentation and excitation/emission. All of the observed emission bands following PF/FD of EEP correspond to either C_2 or CH molecules, indicating conclusively that these species are produced from the parent molecule. It should be noted that not all fragments produced will retain sufficient energy to populate an excited state, that not all excited states will decay radiatively, and that the optics of the experimental setup prohibit the observation of bands of wavelength less than approximately 350 nm; therefore, the current list of observed photofragments may not be comprehensive. Nonetheless, based on the molecular structure of EEP, two photofragmentation pathways are proposed as shown in Fig. 4. In the first, an ethyl radical (C_2H_5) is produced by cleaving one of the two single C–O bonds in the linear EEP chain (see Fig. 4A):



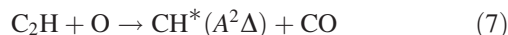
It is noted that the energy of the incident 193 nm photon (6.4 eV) exceeds the bond energy of the C–O bond (~ 3.6 eV), leaving considerable excess energy for subsequent processes. The ethyl radical then subsequently undergoes hydrogen abstraction via collision with other molecules (N_2 , O_2 , or other photofragments) or via photodissociation (using additional 193 nm photons and/or excess energy) until it results in a C_2H (ethynyl) radical. From this point, subsequent hydrogen abstraction (collisional or photochemical) results in the production of an excited C_2 molecule, which can then fluoresce and produce the lines observed corresponding to the C_2 Swan band (example given for the strongest line observed at 516.5 nm):



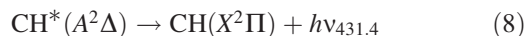
The ethynyl radical has also been shown to react with oxygen in combustion systems to produce an excited CH molecule:²⁹



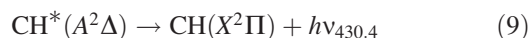
Ethynyl radicals may also react with oxygen atoms generated from the photolysis of diatomic oxygen, a reaction found to have a significantly higher rate constant compared to the reaction shown in Eq. 6:³⁰



The excited CH molecule produced via this pathway will subsequently fluoresce to produce the CH band emission lines as:



and



In the second proposed pathway, the initial photofragmentation of EEP produces a methyl radical (CH_3) by cleaving one of the C–C bonds (~ 3.6 eV) located at either end of the linear parent molecule (see Fig. 4B):



Hydrogen atom abstraction (collisional or photochemical) of the methyl radical then produces an excited CH molecule that will subsequently fluoresce and result in the observed emission lines via Eqs. 8 and 9. The overall scheme is as follows:



Note that the specific state of CH produced prior to fluorescence in the first proposed photofragmentation pathway (Eq. 8) is only one possible excited state; excess energy may result in CH molecules emitting other wavelengths of light corresponding to decay from other excited states throughout the $A^2\Delta \rightarrow X^2\Pi$ and $B^2\Sigma \rightarrow X^2\Pi$ band heads. It should also be noted that alternate detection strategies (i.e., not prompt

emission photofragmentation) have demonstrated that the 193 nm photolysis of several hydrocarbons (CH_4 , C_2H_2 , CH_3COCH_3 , etc.) produce carbon atoms in multiple states (^1D , ^1S , ^3P) as well as carbon ions.^{31,32} CH or CH_2 produced via the pathways previously described may react with these carbons to produce the C_2 molecules observed. Although corroborative data are not available to confirm the above proposed photofragmentation pathways, both are consistent with the production of the observed emission signals corresponding to C_2 and CH molecules, as well as with the relevant bond and photon energies.

Adsorption of EEP on Aerosol Particles. As previously mentioned, if photofragmentation can be used to characterize the interaction of noxious vapors with aerosol particles, it has potential value for the study of heterogeneous chemical reactions in the atmosphere involving these compounds. To test this possibility, four aerosols produced from the nebulization of sodium-rich species solutions were considered, namely, NaCl , a standard solution of Na in HNO_3 , NaOH , and Na_2SO_4 . The integrated sodium photofragmentation emission intensity (full-width) signal at 589.6 nm ($0\text{--}16976\text{ cm}^{-1}$) for the first three sodium-based aerosol species without the presence of EEP is shown in Fig. 5 as a function of the resulting Na concentration produced in the drying chamber. It is expected that small amounts of Na -rich particulates were lost during transport through the diffusion dryer and additional tubing prior to reaching the sample chamber (i.e., reduced Na concentration), although such losses were not quantified; hence, the drying chamber concentration is used as a metric that is proportional to the actual chamber concentration. Identical results were observed for the sodium peak at 589.0 nm ($0\text{--}16973\text{ cm}^{-1}$) for the three Na solutions. However, no atomic Na photofragmentation signal was observed from nebulization of the Na_2SO_4 at any concentration, as discussed below. With the Fig. 5 data, it can be seen that the Na photofragmentation signal corresponding to aerosol particles derived from the desolvation of NaCl , Na dissolved in HNO_3 , and NaOH solutions increases with increasing aerosol concentration. The Na emission peak intensity was observed to increase further with higher Na concentrations (up to $180\text{ }\mu\text{g/L}$) for NaCl - and NaOH -derived sodium-based aerosols (the only two sources examined at higher concentrations), although nonlinearity was observed, as discussed below.

Overall, the Na source-dependency result is not surprising when one considers the energy threshold required to dissociate each of the considered sodium-rich aerosol particles. A 193 nm laser is sufficient to dissociate the Na , NaCl , and NaOH species and leave them in the excited state required for prompt emission photofragmentation, with higher concentrations of particles within the system resulting in the increased observed signal. However, a photofragmentation laser of wavelength less than 179 nm ($>6.9\text{ eV}$) is required to dissociate Na_2SO_4 ; therefore, no signal is observed at any concentration of this aerosol.²⁵ These results are consistent with previous findings in the literature, where photofragmentation of Na_2SO_4 aerosols with a 193 nm (6.4 eV) laser produced only a weak Na emission at very high incident laser energies, attributed to multiphoton interaction.²⁵ In contrast, NaCl and NaOH produced much stronger Na emission even at lower incident laser energies, which was attributed to the differences in bond energy in the context of the incident photon energy. It is also noted that the observed Na signal is approximately linear with

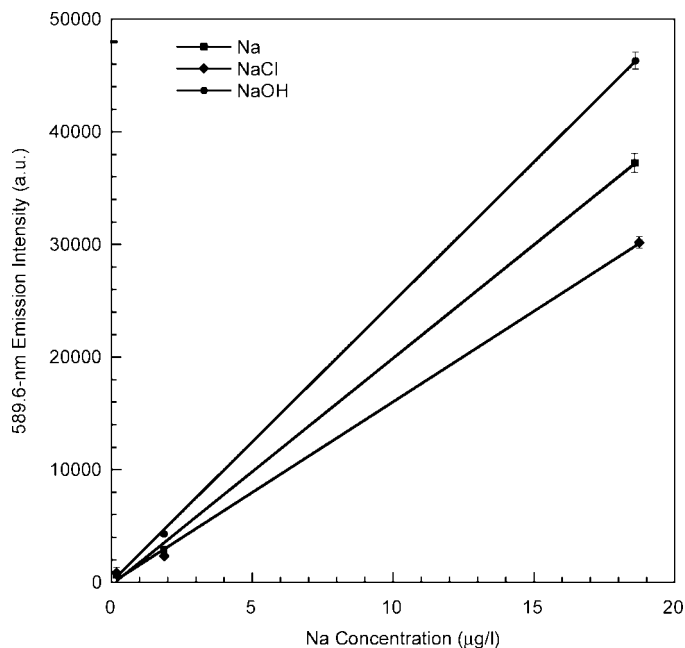


FIG. 5. Full-peak integrated 589.6 nm sodium photofragmentation emission signal as a function of atomic sodium concentration within the mixing chamber (see Fig. 1). The source of sodium atoms corresponds to nebulized solutions of Na (in dilute HNO_3 solution), NaCl , and NaOH , as labeled. Error bars represent plus or minus one standard deviation.

zero intercept for the lower Na concentrations reported in Fig. 5, although the linearity did not persist at the higher Na concentrations. As the Na concentration is increased by the nebulization of higher concentration Na solutions, the mean particle diameter of the resulting aerosol also increases. Because photofragmentation is a surface-weighted process and may not result in complete sampling of the particulate, the effects of particle size on the volume-to-surface area ratio may result in a nonlinear relationship between signal and concentration, as observed with the higher concentrations. However, small aerosol particles may produce a quasi-linear response, as in Fig. 5, due to sufficient penetration and sampling of the particulates. Such size effects should be considered in the context of future quantitative analysis.

To consider the adsorption of EEP onto the sodium-rich aerosol particles, various particulate concentrations were considered for each of the three aerosol species that produce Na emission from 193 nm photofragmentation. Results for the observed EEP signal at the CH band of 431.4 nm are shown in Fig. 6 as a function of the sodium concentration in the nebulized solutions. Similar trends were observed for the CH band at 430.4 nm and the C_2 band at 516.5 nm, namely a decrease in EEP photofragmentation emission intensity with an increase in sodium concentration. As previously mentioned, one of the difficulties inherent with this experimental setup is the loss of signal observed over time due to degradation of the optical windows by the incident UV radiation, notably in the presence of aerosol. To ensure that any drop in signal was a result of EEP interaction with the aerosol and not contamination of optical windows, experiments consisted of taking an initial signal for isolated EEP followed by measurements for each concentration/species of aerosol, and lastly a final signal of isolated EEP. The average percentage reduction in EEP emission intensity, as measured using the 431.4 nm CH

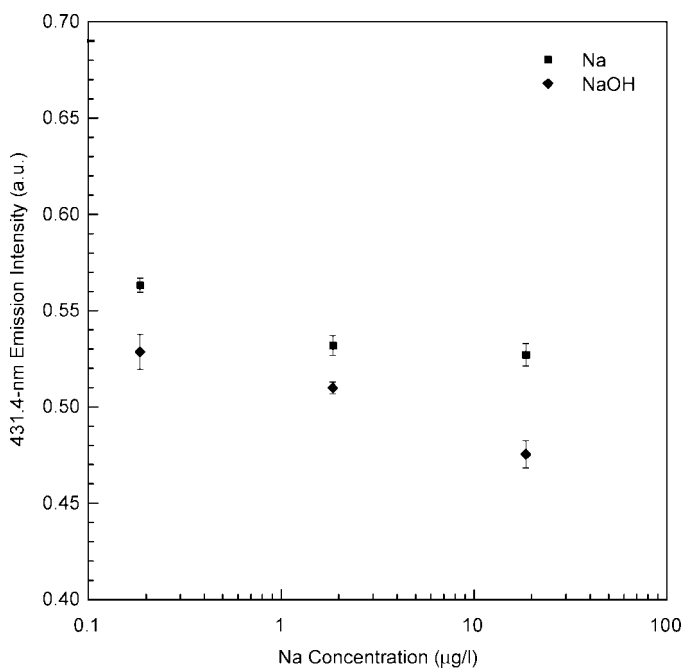


FIG. 6. Normalized EEP photofragmentation signal of the 431.4 nm CH emission line as a function of atomic sodium concentration within the mixing chamber (see Fig. 1). The source of sodium atoms corresponds to nebulized solutions of Na (in dilute HNO₃ solution) and NaOH, as labeled. The signals are normalized to the pure EEP emission intensity (i.e., no sodium aerosol), and the error bars represent plus or minus one standard deviation.

emission line, as a function of sodium aerosol concentration, is shown in Fig. 6. As with the Fig. 5 data, the Na concentration reflects the values in the mixing chamber for the two different sodium sources, namely Na dissolved in HNO₃, and NaOH. The data reveal an average reduction of more than 50% with the introduction of sodium-rich aerosol, with a slight trend of increasing signal reduction with increasing aerosol loading. Note that the volume of co-flow is adjusted to keep the total flow rate through the chamber constant for all conditions, and therefore, this reduction is not due to dilution of the gaseous EEP. In comparison, the average change in the pre- and post-aerosol EEP reference signals was less than 9%; hence, the reductions observed in Fig. 6 are due to the direct interaction of EEP and Na-rich aerosol particulates within the sample chamber. The results for NaCl-based aerosol particles fell within the results obtained for the Na and NaOH data.

For all three EEP bands considered in detail (the two CH bands and the C₂ band), the emission intensity signal was observed to drop significantly with the presence of aerosol species. Increased aerosol loading enhanced the effect, although not greatly, with larger concentrations of aerosol resulting in a greater reduction in the EEP signal. In contrast, the corresponding sodium atomic emission signal (589.0 and 589.6 nm) observed for each of the considered Na species was unaffected (i.e., no change in photofragmentation emission intensity) by the presence of EEP. With the selective loss of EEP-derived emission in the presence of the sodium aerosol, it is proposed that the reduction is the result of EEP adsorption onto the sodium-rich particulates. Accordingly, photofragmentation spectroscopy effectively measures the uptake of EEP onto the aerosol particle surface and may be useful for future

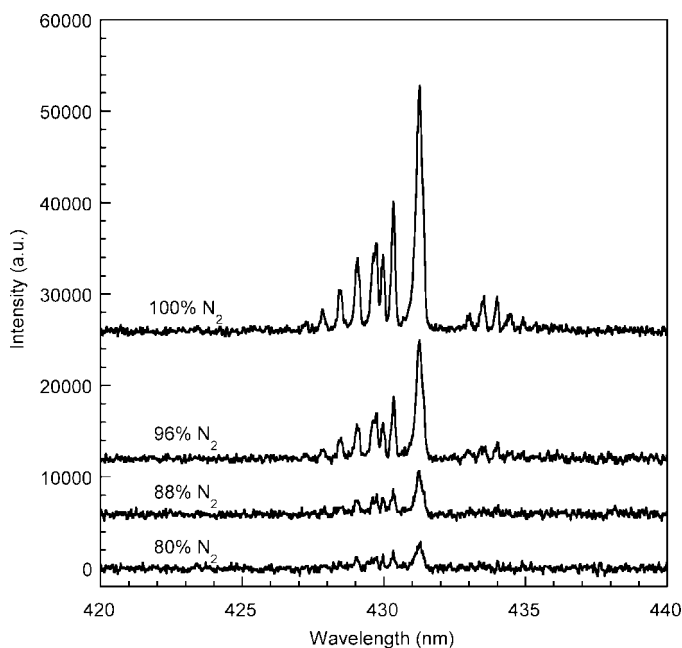


FIG. 7. Photofragmentation spectra of EEP recorded in various nitrogen/oxygen mixtures showing the CH emission bands. The nitrogen percentage is presented for each spectrum, with the balance of the mixture oxygen. All spectra have the same scale and have been shifted vertically for clarity.

laboratory studies of adsorption kinetics as related to heterogeneous aerosol chemistry.

Oxygen Quenching of EEP Signal. During the course of experimentation, it was discovered that the EEP signal observed with both CH and C₂ bands was significantly lower when using a carrier gas of air as opposed to pure N₂, whereas the sodium signal observed from the aerosol species was unaffected by the presence of oxygen. To quantify this observation, photofragmentation studies were carried out using mixtures consisting of N₂ and O₂ at various concentrations, ranging from pure nitrogen to 80% nitrogen, 20% oxygen (consistent with the composition of air). Higher concentrations of oxygen were not considered given the potential flammability of the EEP vapor in more oxygen-rich environments. The spectra observed for EEP around the 430 nm band are shown in Fig. 7. Similar results were observed for spectra recorded using the C₂ Swan band near 516 nm. Overall, a dramatic decrease in signal for intensity bands in both the 430 nm range (CH) and the 516 nm range (C₂) is observed with increased concentration of oxygen, whereas the sodium signal was unaffected by the change in O₂ percentage. The observed C₂ band at 516 nm nearly completely disappears with only a modest concentration of oxygen present, 4%.

To quantify the effects of oxygen as a quenching species, Stern–Volmer plots using the intensity of the EEP photofragmentation signals were created. The information obtained from the Stern–Volmer plot derives from the relationship of the quantum efficiency of a fluorescent species (Φ_F^0) to the quantum efficiency of the same fluorescent species in the presence of a quencher (Φ_F) of a given concentration [Q] as a function of the Stern–Volmer quenching constant (K_q) as:³³

$$\frac{1}{\Phi_F} = \frac{1}{\Phi_F^0} + \frac{K_q}{\Phi_F^0} [Q] \quad (12)$$

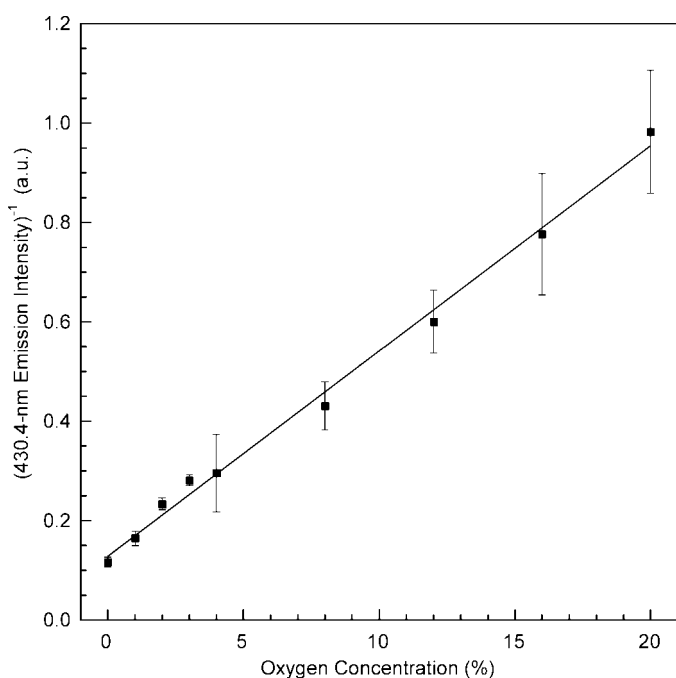


FIG. 8. Stern–Volmer plot of the inverse of the 430.4 nm CH photofragmentation emission signal as a function of the oxygen concentration in a nitrogen balance. Error bars represent plus or minus one standard deviation.

A linear relationship between the inverse of the observed fluorescence and the concentration of the quenching species indicates that the species is indeed acting as a fluorescence quencher. The Stern–Volmer plot for the emission originating from the CH band at 430.4 nm is shown in Fig. 8, with similar results observed for the CH band at 431.4 nm and the C₂ band at 516.5 nm. For all of the EEP bands, the inverse of the integrated peak revealed a linear relationship with the concentration of oxygen, indicative that oxygen is an effective quenching species. By converting the percentage of oxygen to molarity, the Stern–Volmer quenching constant can be calculated for each of the observed bands, yielding the values of K_q : 7.2 L/mol at 430.4 nm, 7.8 L/mol at 431.4 nm, and 14.5 L/mol at 516.5 nm. Finally, the second-order rate constant for external quenching may be calculated directly from the Stern–Volmer quenching constant K_q and the fluorescence decay time constant in the absence of the external quencher (i.e., in pure nitrogen). Using the Table I time constants, the second-order rate constants for external quenching by diatomic oxygen were calculated as: 2.2×10^8 L mol⁻¹ s⁻¹ at 430.4 nm; 1.3×10^8 L mol⁻¹ s⁻¹ at 431.4 nm; and 3.5×10^8 L mol⁻¹ s⁻¹ at 516.5 nm.

The effect of oxygen quenching on the time-resolved measurements of EEP were also considered. In the case of quenching, those species acting as static quenchers (e.g., a non-

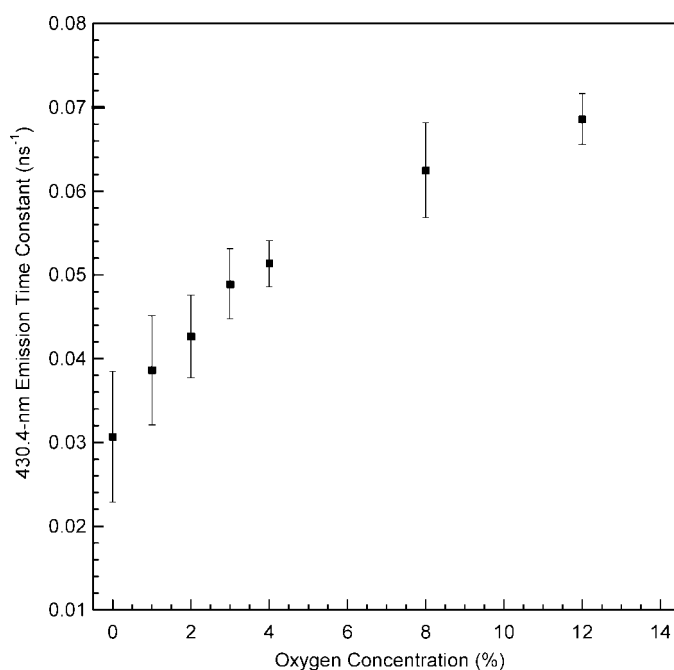


FIG. 9. Calculated time constant for an exponential decay of the 430.4 nm CH photofragmentation emission signal as a function of the oxygen concentration in a nitrogen balance. Error bars represent plus or minus one standard deviation.

fluorescent complex is formed between quencher and fluorophore) do not affect the fluorescence lifetime, whereas those species participating in dynamic quenching (e.g., collisions between the quencher and the fluorophore that result in non-radiative energy transfer and decay to the ground state) do result in a reduction in the fluorescence lifetime.³³ A decrease in fluorescence lifetime was observed in the EEP signal from both CH and C₂ photofragments, with an increased concentration of O₂ resulting in a reduction in the fluorescence lifetime. As with the observed sodium emission intensity measurements, oxygen was observed to have no effect on the fluorescence lifetime of the sodium signal. To quantify the result of the CH and C₂ lifetime data, the decay time constant (ns⁻¹) for each observed band was calculated by fitting an exponential decay to the recorded intensity signal as a function of time (see Table I), noting that a larger decay time constant corresponds to a more rapid decay of the photofragmentation signal. The time constant calculated in this manner for the 430.4 nm CH band as a function of oxygen concentration in a nitrogen balance is shown in Fig. 9, with similar results observed for the other EEP photofragmentation bands. It can be observed that in addition to the EEP signal showing a drop in intensity with increased oxygen concentration, as previously discussed, the decay time

TABLE I. Calculated decay time constants (ns⁻¹) for CH and C₂ bands as a function of oxygen percentage in the carrier gas. Note that a larger decay time constant indicates a more rapid decay in the fluorescence signal.

Wavelength	Percentage of Oxygen								
	0%	1%	2%	3%	4%	8%	12%	16%	20%
CH 430.4 nm	0.0307	0.0386	0.0427	0.0489	0.0514	0.0625	0.0686	0.0669	0.0745
CH 431.4 nm	0.0169	0.0209	0.0255	0.0288	0.0354	0.0495	0.0559	0.0634	0.0675
C ₂ 516.5 nm	0.0242	0.0275	0.0292	0.0316	0.0305	0.0345	0.0326	0.0309	0.0303

TABLE II. Calculated kinetic rates for various decay mechanisms of the excited CH molecule. The forward rate constant is given by the equation $k = AT^n \exp(-E_A/R_u T)$, where T is the temperature [K], E_A is the activation energy [kJ/gmol], and R_u is the universal gas constant. The A , n , and E_A values are taken from Ref. 29.

Reaction	Forward rate coefficients			Forward rate constant (k)
	A	n	E_A	($T = 293$ K)
$\text{CH}(A^2\Delta) \rightarrow \text{CH}(X^2\Pi) + h\nu$	1.90×10^6	0	0	1.9×10^6 [s ⁻¹]
$\text{CH}(A^2\Delta) + M \rightarrow \text{CH}(X^2\Pi) + M$	4.00×10^{10}	0.50	0	6.8×10^{11} [m ³ mol ⁻¹ s ⁻¹]
$\text{CH}(A^2\Delta) + \text{O}_2 \rightarrow \text{CH}(X^2\Pi) + \text{O}_2$	2.40×10^{12}	0.50	0	4.1×10^{13} [m ³ mol ⁻¹ s ⁻¹]

constant also increases, indicating a faster decay in signal intensity and therefore a shorter fluorescence lifetime.

In view of these results it is interesting to consider the behavior of $\text{CH}^*(A^2\Delta)$ as reported in a methane oxidation mechanism,²⁹ both alone and in the presence of other species, a summary of which is provided in Table II. Both oxygen and other species can interact with the excited CH molecule to result in non-fluorescent decay to the ground state; however, the calculated value of the forward rate constant for the reaction with oxygen (4.1×10^{13} m³ mol⁻¹s⁻¹ at $T = 293$ K) is two orders of magnitude greater at the same temperature than that observed for reaction with any other species, for example, nitrogen (6.8×10^{11} m³ mol⁻¹s⁻¹ at $T = 293$ K). The oxygen quenching reaction is also seven orders of magnitude greater than the rate at which the excited species will spontaneously fluoresce to return to the ground state (1.9×10^6 s⁻¹ at $T = 293$ K). This increased reaction rate is consistent with the quenching behavior observed in the photofragmentation system in the presence of oxygen and may mitigate the potential contributions of Eqs. 6 and 7. Although N₂ molecules or EEP photofragments may collide with the excited CH molecules and result in non-fluorescent decay, the quenching rate of reaction between oxygen and the excited CH molecules is orders of magnitude faster, resulting in both the reduced magnitude of fluorescent signal (due to reduced quantum efficiency) and the shorter lifetime seen in time-resolved measurements.

CONCLUSIONS

The PF/FD technique has been demonstrated to have potential as a possible monitoring technique for VOC solvents and as a tool for the *in situ* study of heterogeneous chemistry involving these species and their interaction with aerosol particles. Based on the photofragment bands observed from EEP (corresponding to CH and C₂ molecules), photofragmentation pathways for that species are proposed for the first time. An investigation of the atomic sodium PF/FD signal observed for various sodium aerosol systems yields an increase in intensity with increased aerosol concentration for species with bond energy sufficiently low enough for photofragmentation at 193 nm, a result consistent with previous studies.²⁵ A reduction of the EEP signal is seen in the presence of particles as a result of vapor loss via surface adsorption, demonstrating proof-of-concept for PF/FD as a possible tool for the study of uptake rates of gaseous oxygenated hydrocarbons onto particulate matter, a precursor of heterogeneous chemical reaction. An investigation into the effect of oxygen on the observed EEP signal has demonstrated that oxygen acts as a dynamic quencher for the photofragments generated in PF/FD analysis of EEP, with increased oxygen concentration resulting in both a decrease in observed intensity and a shortening of the

fluorescence lifetime of the observed photofragments. The implication of this result is that any efforts to quantitatively determine solvent concentrations, for example in the applications of environmental or emission monitoring where oxygen concentration may vary, must take carrier gas composition into account when performing calibration.

ACKNOWLEDGMENTS

P.S.D. was supported in part by the National Science Foundation Graduate Fellowship program. D.W.H. would like to thank Dr. Jean Andino (Arizona State University) for bringing the interesting problem of *in situ* monitoring of VOCs and heterogeneous chemistry to our attention. The authors would also like to thank one of the reviewers for bringing to our attention additional reaction mechanisms and pathways for consideration.

1. M. L. Boeglin, D. Wessels, and D. Henshel, *Environ. Res.* **100**, 242 (2006).
2. P. Irigaray, J. A. Newby, R. Clapp, L. Hardell, V. Howard, L. Montagnier, S. Epstein, and D. Belpomme, *Biomed. Pharm.* **61**, 640 (2007).
3. K. Katsouyanni, *Brit. Med. Bull.* **68**, 143 (2003).
4. Y.-H. Shih and M.-S. Li, *J. Hazard. Mater.* **154**, 21 (2008).
5. S. T. Leong, S. Muttamara, and P. Laortanakul, *Atmos. Environ.* **36**, 3495 (2002).
6. M. O. Rodgers, K. Asai, and D. D. Davis, *Appl. Opt.* **19**, 3597 (1980).
7. J. B. Simeonsson and R. C. Sausa, *Appl. Spectrosc. Rev.* **31**, 1 (1996).
8. J. B. Simeonsson and R. C. Sausa, *Trends Anal. Chem.* **17**, 542 (1998).
9. M. P. P. Monterola, Ph.D. Thesis, University of Florida, Gainesville, Florida (2007).
10. O. Johansson, J. Bood, M. Aldén, and U. Lindblad, *Appl. Spectrosc.* **62**, 66 (2008).
11. R. C. Oldenborg and S. L. Baugheum, *Anal. Chem.* **58**, 1430 (1986).
12. B. L. Chadwick, G. Domazetis, and R. J. S. Morrison, *Anal. Chem.* **67**, 710 (1995).
13. B. L. Chadwick and R. J. S. Morrison, *J. Chem. Soc. Faraday Trans.* **91**, 1931 (1995).
14. B. L. Chadwick, P. G. Griffin, and R. J. S. Morrison, *Appl. Spectrosc.* **51**, 990 (1997).
15. S. G. Buckley, R. F. Sawyer, C. P. Koshland, and D. Lucas, *Combust. Flame* **128**, 435 (2002).
16. J. B. Simeonsson, S. A. Elwood, M. Niebes, R. Carter, and A. Peck, *Anal. Chim. Acta* **397**, 33 (1999).
17. C. S. McEnally, R. F. Sawyer, C. P. Koshland, and D. Lucas, *Appl. Opt.* **33**, 3977 (1994).
18. J. B. Halpern, W. M. Jackson, and V. McCrary, *Appl. Opt.* **18**, 590 (1979).
19. S. G. Buckley, C. J. Damm, W. M. Vitovec, L. M. Sgro, R. F. Sawyer, C. P. Koshland, and D. Lucas, *Appl. Opt.* **37**, 8382 (1998).
20. H. K. Haak and F. Stuhl, *J. Phys. Chem.* **88**, 2201 (1984).
21. J. S. Schendel, R. E. Stickel, C. A. van Dijk, S. T. Sandholm, D. D. Davis, and J. D. Bradshaw, *Appl. Opt.* **29**, 4924 (1990).
22. C. J. Damm, D. Lucas, R. F. Sawyer, and C. P. Koshland, *Appl. Spectrosc.* **55**, 1478 (2001).
23. C. B. Stipe, D. Lucas, C. P. Koshland, and R. F. Sawyer, *Appl. Opt.* **44**, 6537 (2005).
24. M. Hidalgo Núñez, P. Cavalli, G. Petrucci, and N. Omenetto, *Appl. Spectrosc.* **54**, 1805 (2000).
25. M. Hidalgo Núñez and N. Omenetto, *Appl. Spectrosc.* **55**, 809 (2001).
26. J. H. Choi, C. B. Stipe, C. P. Koshland, R. F. Sawyer, and D. Lucas, *J. Appl. Phys.* **97**, 124315/1 (2005).
27. O. F. Swenson, J. A. Williams, R. Wells, T. Tipton, S. Baxley, and S.

- Markgraf, Proceedings of the SPIE Conference on Advanced Sensors and Monitors for Process Industries and Environment **3535**, 244 (1998).
28. TSI Model 3076 Operation and Service Manual (TSI, Shoreview, MN, February, 2008).
29. M. Frenklach, H. Wang, and M. J. Rabinowitz, *Prog. Energy Combust.* **18**, 47 (1992).
30. K. Devriendt, H. Van Look, B. Ceursters, and J. Peeters, *Chem. Phys. Lett.* **261**, 450 (1996).
31. R. C. Sausa, A. J. Alfano, and A. W. Miziolek, *Appl. Opt.* **26**, 3588 (1987).
32. R. L. Whetten, K.-J. Fu, R. S. Tapper, and E. R. Grant, *J. Phys. Chem.* **87**, 1484 (1983).
33. J. D. Ingle, Jr. and S. R. Crouch, *Spectrochemical Analysis* (Prentice-Hall Inc., New Jersey, 1988), p. 339–344.